This is the accepted manuscript made available via CHORUS. The article has been published as:

Band-to-band transitions, selection rules, effective mass, and excitonic contributions in monoclinic β-Ga_{2}O_{3}

Alyssa Mock, Rafał Korlacki, Chad Briley, Vanya Darakchieva, Bo Monemar, Yoshinao Kumagai, Ken Goto, Masataka Higashiwaki, and Mathias Schubert

Phys. Rev. B **96**, 245205 — Published 29 December 2017

DOI: 10.1103/PhysRevB.96.245205

Band-to-band transitions, selection rules, effective mass and excitonic contributions in monoclinic β-Ga_2O_3

Alyssa Mock,[1,*] Rafał Korlacki,[1] Chad Briley,[1] Vanya Darakchieva,[2] Bo Monemar,[2,3] Yoshiano Kumagai,[4,3] Ken Goto,[4,5] Masataka Higashiwaki,[6] and Mathias Schubert[1,2,7]

[1] *Department of Electrical and Computer Engineering and Center for Nanohybrid Functional Materials, University of Nebraska-Lincoln, Lincoln, NE 68588, USA*
[2] *Department of Physics, Chemistry, and Biology (IFM), Linköping University, SE 58183, Linköping, Sweden*
[3] *Global Innovation Research, Tokyo University of Agriculture and Technology, Koganei, Tokyo, Japan*
[4] *Department of Applied Chemistry, Tokyo University of Agriculture and Technology, Koganei, Tokyo, Japan*
[5] *Tamura Corporation, Sayama, Saitama, Japan*
[6] *National Institute of Information and Communications Technology, Koganei, Tokyo, Japan*
[7] *Leibniz Institute for Polymer Research, Dresden, Germany*

(Dated: November 17, 2017)

We employ an eigen polarization model including the description of direction dependent excitonic effects for rendering critical point structures within the dielectric function tensor of monoclinic β-Ga_2O_3 yielding a comprehensive analysis of generalized ellipsometry data obtained from 0.75 eV–9 eV. The eigen polarization model permits complete description of the dielectric response. We obtain, for single-electron and excitonic band-to-band transitions, anisotropic critical point model parameters including their polarization eigenvectors within the monoclinic lattice. We compare our experimental analysis with results from density functional theory calculations performed using the Gaussian-attenuation-Perdew-Burke-Ernzerhof hybrid density functional. We present and discuss the order of the fundamental direct band-to-band transitions and their polarization selection rules, the electron and hole effective mass parameters for the three lowest band-to-band transitions, and their excitonic contributions. We find that the effective masses for holes are highly anisotropic and correlate with the selection rules for the fundamental band-to-band transitions. The observed transitions are polarized close to the direction of the lowest hole effective mass for the valence band participating in the transition.

I. INTRODUCTION

Single crystalline group-III sesquioxides are currently at the forefront of research for applications in electronic and optoelectronic devices due to unique physical properties. Such conductive oxides, including tin doped In_2O_3 or Ga_2O_3, can be utilized as transparent thin film electrodes for various devices such as photovoltaic cells[1], flat panel displays[2], smart windows[1,3], and sensors[4]. The highly anisotropic monoclinic β-gallia crystal structure (β phase) is the most stable crystal structure among the five phases (α, β, γ, δ, and ϵ) of Ga_2O_3 (Fig. 1)[5,6]. It belongs to the space group 12 and has base center monoclinic lattice. Ga_2O_3 shows potential for use in transparent electronics and high energy photonic applications due to its large band gap of 4.7-4.9 eV[7–10].

Precise and accurate knowledge of the band gap energies, band-to-band transitions, their polarization selection rules and energetic order, and the resulting anisotropy in the dielectric function are important physical properties in low symmetry materials. Electronic band-to-band transitions cause critical point (CP) features in the joint density of states, which result in CP structures in the dielectric function[11]. Parameters of a appropriately selected physical model dielectric function (MDF) yield access to CP parameters such as band-to-band transition energies and polarization selection rules, which allow for direct comparison with results both from experiment, e.g., optical absorption and reflectance measurements, as well as from theory, e.g., density functional theory (DFT) band structure calculations.[11] A suitable and precise technique to determine the complex dielectric function tensor from arbitrarily anisotropic materials is generalized spectroscopic ellipsometry (GSE)[12–24]. MDF approaches were used successfully to quantify anisotropy and band-to-band transitions for many different types of materials[12,15–19,21,25].

Fundamental band-to-band transitions in β-Ga_2O_3 have been investigated using density functional theory (DFT) calculations[9,10,26–28], optical absorption[26], reflection[29,30], and ellipsometry[8,9]. Due to monoclinic symmetry, the polarization of a given band-to-band transition may not necessarily align with any of the high symmetry crystal axes. The formation of excitons upon the optical excitation of a band-to-band transition strongly modifies the frequency dependence of the dielectric response in semiconductors[11]. Thus, in order to accurately determine the transition energies, the excitonic contribution must be accounted for. For β-Ga_2O_3, there has been significant discrepancies in reported properties of the fundamental band-to-band transitions. Ricci *et al.*, ignoring excitonic effects, recently showed optical absorption anisotropy in β-Ga_2O_3 with the lowest onset of absorption occurring with polarization in the **a-c** plane at 4.5-4.6 eV[26]. For polarization along the crystal axis **b** the absorption onset was unambiguously shifted by 0.2 eV

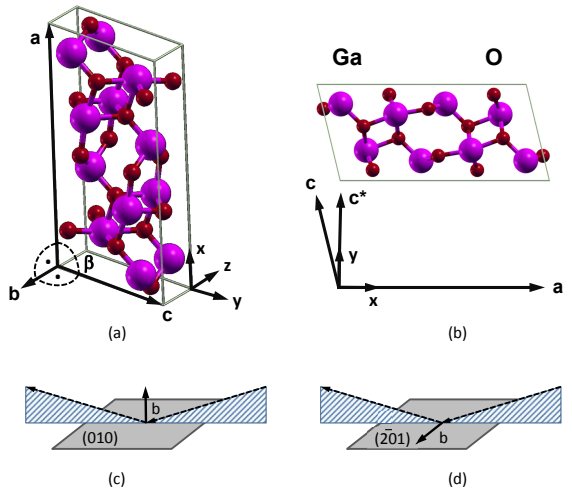

FIG. 1. (a) Unit cell of β-Ga_2O_3 detailing crystallographic and laboratory coordinate systems. (b) Description of the orthogonal laboratory coordinate system within the monoclinic **a-c** plane. Axis **c*** is chosen for convenience parallel to laboratory axis y, and orthogonal to both **a** and **b**. (c) and (d): Ellipsometry plane of incidence for the (010) and ($\bar{2}$01) surfaces of β-Ga_2O_3 single crystals used in this work, respectively. Samples are rotated stepwise around their surface normal to different measurement positions (See Sect. III A). In (c), axis **b** is parallel to the plane of incidence, and in (d) parallel to the sample surface regardless of sample rotation.

towards shorter wavelength. Onuma *et al.* investigated polarized transmittance and reflectance spectra[30]. As a result of their investigations, an indirect gap band-to-band transition around 4.43 eV and a direct gap transition around 4.48 eV parallel to the **c** axis were proposed, without considering excitonic effects. Sturm *et al.* considered contributions from both bound and unbound Wannier-type excitons[31–33] and reported the lowest direct gap band-to-band transition at approximately 4.88 eV, polarized within the **a-c** plane nearly parallel to **c**. Furthmüller and Bechstedt presented quasiparticle band structures and density of states of β-Ga_2O_3 obtained from DFT combined with Hedin's GW approximation for single-particle excitations[10]. The lowest transition energy was determined by this approach to be around 5.04 eV, with polarization mainly along the **c** axis in the monoclinic **a-c** plane.

A comprehensive paper by Furthmüller and Bechstedt[10] as well as papers by other authors[9,10,26–28] report computational studies using hybrid functionals of Heyd, Scuseria, and Ernzerhof (HSE)[34] for β-Ga_2O_3. In this work, we use Gau-PBE which to the best of our knowledge has not yet been used for band structure calculation of β-Ga_2O_3. The primary purpose of our DFT calculations is to identify band-to-band transitions and to calculate parameters of CP transitions, and compare these with contributions to the experimental dielectric function of β-Ga_2O_3. We note that for our purpose the band structure calculations at the hybrid HF-DFT level are sufficient.[35,36]

Sturm *et al.*[9] recently investigated the NIR-UV dielectric function tensor elements of β-Ga_2O_3. Schubert et al.[23,37] adapted the concept of the dielectric eigen displacement polarizations in the Born and Huang model[38] to develop a monoclinic CP-MDF for phonon excitations in β-Ga_2O_3. Sturm *et al.*[8] provided a CP analysis for β-Ga_2O_3 extending the Born and Huang model[38] to interband excitations. In their analysis, Sturm *et al.* assumed that the exciton binding energy parameter is the same for all band-to-band transitions, and its value was assumed as well rather than determined by experiment. In this present work, we perform a different CP-MDF analysis and determine the excitonic contributions for the lowest transitions independently. Our results for the band-to-band transition parameters differ in detail from those reported by Sturm *et al.*. We provide additional information on band-to-band transitions into the VUV range not previously reported. We further provide and discuss effective mass parameters determined in our DFT analysis for the topmost valence and lowest conduction bands.

II. THEORY

A. Mueller matrix generalized ellipsometry

Optically anisotropic materials necessitate the application of generalized ellipsometry[12,18,19,39–41]. Multiple β-Ga_2O_3 samples cut at different angles from the same crystal are investigated using Mueller matrix generalized ellipsometry (MMGE) at multiple angles of incidence and multiple sample azimuthal angles, and all data are then analyzed simultaneously. For model calculations we use the substrate-ambient approximation, where the single crystalline β-Ga_2O_3 samples correspond to the half-infinite substrate[14]. We assign coordinate relations between laboratory coordinate axes ($\hat{x}$,$\hat{y}$,$\hat{z}$) and crystallographic axes (**a**, **b**, **c**).[23] We choose the $\hat{z}$ axis of the laboratory coordinate system to be normal to the sample surface, thereby defining the sample surface as the laboratory $\hat{x}$-$\hat{y}$ plane. By our choice, the (x,y,z) system is described in Fig.1 with respect to the crystal structure. Euler angles (ϕ, θ, and ψ) are then determined to describe angular rotations necessary to relate (x,y,z) with ($\hat{x}$,$\hat{y}$,$\hat{z}$). Effects of finite roughness always present on the nanoscale when measuring polished crystal surfaces must be accounted for. An effective medium approximation (EMA) approach is commonly used to mimic the effect of a very thin effective layer with thickness much smaller than all wavelengths for data analysis[42]. Rigorous treatment of the combination of roughness and anisotropy has not been investigated yet, hence, an isotropic averaging approach was employed here. Thus, our roughness layer model was calculated by averaging all four dielectric tensor elements and then added together in the EMA approach assuming 50% void.

B. Monoclinic dielectric tensor description

For materials with monoclinic symmetry four independent dielectric tensor elements are needed[23,43]. With the coordinate choices in Fig. 1 we select the dielectric tensor cross-term element ε_{xy} as the fourth independent element

$$\varepsilon = \begin{pmatrix} \varepsilon_{xx} & \varepsilon_{xy} & 0 \\ \varepsilon_{xy} & \varepsilon_{yy} & 0 \\ 0 & 0 & \varepsilon_{zz} \end{pmatrix}. \quad (1)$$

C. Eigen polarizability critical point model

We adopt the concept of the Born and Huang model and consider electronic contributions to the dielectric response of monoclinic β-Ga_2O_3 as the result of eigen dielectric displacement processes. Each individual contribution l is characterized by a CP model function, $\varrho_l(\omega)$ and its eigen dielectric polarizability unit vector, $\hat{e}_l$. The same approach was adopted by Schubert *et al.*[23] and Sturm *et al.*[8] for analysis of GSE data for FIR-IR and NIR-VUV spectral regions, respectively, as follows:

$$\varepsilon(\omega) = \sum_{l=0}^{N} \varrho_l(\omega)(\hat{e}_l \otimes \hat{e}_l). \quad (2)$$

When l=0, the quasi-static ($\omega \rightarrow 0$) dielectric tensor dyadic $\hat{\varepsilon}_{\mathrm{DC}}$ is determined. For monoclinic materials the tensor can be described according to:

$$\varepsilon_{xx} = \varepsilon_{\mathrm{DC},xx} + \sum_{j=1}^{m} \varrho_j \cos^2\alpha_j, \quad (3a)$$

$$\varepsilon_{yy} = \varepsilon_{\mathrm{DC},yy} + \sum_{j=1}^{m} \varrho_j \sin^2\alpha_j, \quad (3b)$$

$$\varepsilon_{xy} = \varepsilon_{\mathrm{DC},xy} + \sum_{j=1}^{m} \varrho_j \cos\alpha_j \sin\alpha_j, \quad (3c)$$

$$\varepsilon_{zz} = \varepsilon_{\mathrm{DC},zz} + \sum_{k=1}^{n} \varrho_k, \quad (3d)$$

$$\varepsilon_{xz} = \varepsilon_{yz} = 0, \quad (3e)$$

with α_j equal to the angle of the shear projection into the **a-c** plane and m,n equal to the number of CP contributions in the **a-c** plane and **b** direction, respectively.

a. Fundamental band-to-band transitions: We use photon energy ($\hbar\omega$) dependent functions described by Higginbotham, Cardona and Pollak[44] (HCP) for rendering electronic contributions at 3-dimensional Van-Hove singularities ("M_0"-type CP in Adachi's CP composite approach[45]):

$$\varepsilon(E) = AE^{-1.5}\{\chi^{-2}[2-(1+\chi)^{0.5}-(1-\chi)^{0.5}]\}, \quad (4)$$

with $\chi = (\hbar\omega + iB)/E$, and A, E, and B are, respectively, amplitude, transition energy, and broadening parameters, and $i^2 = -1$. Our choice is directed by inspection of the symmetry and band curvatures for the lowest band-to-band transitions observed in our DFT calculations.

b. Excitonic contributions at fundamental band-to-band transitions: The contributions to the dielectric function due to exciton absorption arise from two parts, one from bound states and another from continuum states[11,46,47]. For Wannier-type excitons, Tanguy developed model functions for parabolic bands taking into account bound and unbound states[31,33,48]. These functions, strictly valid for parabolic bands and isotropic materials only, were used by Sturm *et al.*[8] for analysis of GSE data from β-Ga_2O_3. In their work, Sturm *et al.* did not determine the exciton binding energy parameter from using the Tanguy model[31,33,48] approach. In our present work, and because the dominant contribution to exciton absorption processes in direct-band gap semiconductors is the ground state (n=1) transition[11,46], we employ a single Lorentz oscillator with non-symmetric broadening to account for, and to spectrally locate the ground state excitonic contribution, thereby further following Adachi's CP composite approach[45]

$$\varepsilon = \frac{A^2 - ib\hbar\omega}{E^2 - (\hbar\omega)^2 - iB\hbar\omega}, \quad (5)$$

with A, E, B, and b are, respectively, amplitude, energy, broadening, and asymmetric broadening parameter, respectively.

c. Above-band gap band-to-band transitions: At photon energies far above the band gap, multiple transitions originating at multiple points in the Brillouin zone often overlap, and CP features due to individual transitions cannot be differentiated by experiment. Hence, broadened Lorentzian or Gaussian oscillators are often used to account for broad CP features typical for above-band gap spectra.[11,45,49] Here, we use the same anharmonic broadened functions as in Eq. 5.

d. Higher energy band-to-band transitions: Transitions above the spectral range investigated here contribute to the overall lineshape of the dielectric functions at wavelengths within the investigated spectral range. Such higher energy contributions are usually accounted for by Gaussian broadened oscillator functions:[11,45,49]

$$\varepsilon_2(\hbar\omega) = A(e^{-(\frac{\hbar\omega - E}{\sigma})^2} - e^{-(\frac{\hbar\omega + E}{\sigma})^2}). \quad (6)$$

$$\sigma = \frac{B}{2\sqrt{ln(2)}},$$

where amplitude A, center energy E, and broadening B are adjustable parameters. The real part, ε_1, is obtained by the Kramers-Kronig integration[50]:

$$\varepsilon_1(\zeta) = \frac{2}{\pi} P \int_0^{\infty} \frac{\xi\varepsilon_2(\xi)}{\xi^2 - \zeta^2} d\xi. \quad (7)$$

Note that each non-trivial sum in Eqs. 3 satisfies the Kramers-Kronig integral condition[23,37,51], and which can be set as additional side condition during the CP-MDF analysis.

III. METHODS

Bulk single crystalline β-Ga_2O_3 was grown by Tamura Corp., Japan by the edge-defined film fed growth process as described in Refs. 52–54. Samples were then cut at different orientations to the dimensions of 650 μm × 10 mm × 10 mm, and then polished on one side. In this paper we investigate a (010) and a $(\bar{2}01)$ surface.

A. Generalized Spectroscopic Ellipsometry

Mueller matrix generalized spectroscopic ellipsometry data were collected from 133 nm to 1690 nm. The vacuum-ultra-violet (VUV) measurements were obtained using a rotating-analyzer ellipsometer with an automated compensator function (VUV-VASE, J.A. Woollam Co., Inc.). Data were acquired at three angles of incidence (Φ_a=50°, 60°, 70°), and at several azimuthal angles by manually rotating the sample about the sample normal in steps of ≈45°. Note that in the VUV range, due to limitations of the instrument, no elements in the 4^{th} row of the Mueller matrix are available. Measurements from the near-infrared to near ultraviolet (NIR-NUV) were performed using a dual-rotating compensator ellipsometer (RC2, J.A. Woollam Co., Inc.) allowing for the determination of the complete 4×4 Mueller matrix. Measurements were taken at three angles of incidence (Φ_a=50°, 60°, 70°), and at different orientations by auto-rotating the sample by steps of 15° beginning at the same azimuthal orientation as in the VUV measurements. All model calculations were conducted using WVASE32^{TM} (J. A. Woollam Co., Inc.).

B. Density Functional Theory

Density functional theory (DFT) code Quantum ESPRESSO (QE)[55] was used for calculations of the band structure and band to band transitions. The primitive cell of β-Ga_2O_3, with vectors $p_1 = (a-b)/2$ and $p_2 = (a+b)/2$, consisting of six oxygen and four gallium atoms was used, and the initial atomic positions and parameters of the unit cell were taken from Ref. 56. The atoms were represented by norm-conserving pseudopotentials from the QE library; the pseudopotential for gallium did not include the $3d$ electrons in the valence configuration. Structure relaxation was performed to force levels less than 10^{-5} Ry/bohr using the exchange-correlation functional of Perdew, Burke and Ernzerhof (PBE).[57] A 4×4×4 regular shifted Monkhorst-Pack grid was used for sampling of the Brillouin zone[58]. A convergence threshold of 10^{-12} was used to reach self-consistency with a large electronic wavefunction cutoff of 100 Ry. The resulting lattice parameters obtained are shown in Tab. II in comparison with results from previously reported studies using GGA-DFT methods. We find very good agreement between our values and those reported previously.

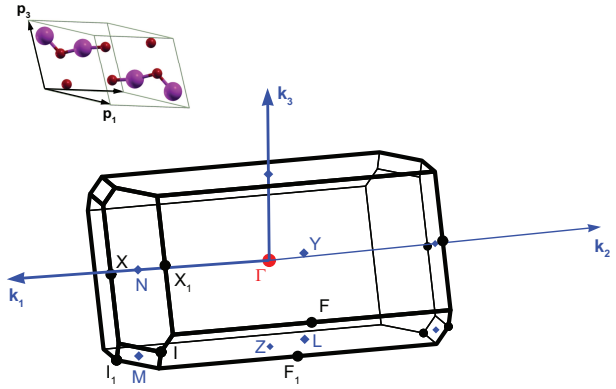

FIG. 2. (Color online) The primitive cell and corresponding Brillouin zone used for plotting the band structure of β-Ga_2O_3. p_1, p_2, and p_3 denote axes of the primitive cell (p_3 not labeled for better clarity of the diagram); k_1, k_2, k_3 denote axes of the first Brillouin zone in the reciprocal space. Labeling of high symmetry points as proposed by Setyawan and Curtarolo[61].

TABLE I. Example coordinates of the high symmetry points in the Brillouin zone. Note that one can draw four symmetry-equivalent paths, i.e., one for each irreducible BZ.

Label	Coordinates for BZ in Fig. 2
Γ	[0,0,0]
Y	[1/2,1/2,0]
F	[1-ζ,1-ζ,η-1]
L	[1/2,1/2,-1/2]
I	[ϕ,1-ϕ,-1/2]
I_1	[1-ϕ,ϕ-1,-1/2]
Z	[0,0,-1/2]
F_1	[ζ,ζ,-η]
X_1	[ψ,1-ψ,0]
X	[1-ψ,ψ-1,0]
N	[1/2,0,0]
M	[1/2,0,-1/2]
Variables:	$\zeta = [2 + (a/c)\cos(\beta)]/[4\sin^2(\beta)] = 0.39715$
	$\eta = 1/2 - 2\zeta(c/a)\cos(\beta) = 0.58937$
	$\psi = 3/4 - b^2/[4a^2\sin^2(\beta)] = 0.7336$
	$\phi = \psi - (3/4 - \psi)(a/c)\cos(\beta) = 0.74181$

The structure fully relaxed at the PBE level was used for electronic structure calculations employing the hybrid Gau-PBE functional.[59,60] This calculation was performed with a 6×6×6 Γ-centered Monkhorst-Pack grid (after testing the convergence with respect to the grid of k-points up to 8×8×8), and with otherwise the same parameters as for the preceding PBE calculations. The converged Gau-PBE wavefunction was used to analyze the band structure.

Fig. 2 shows the Brillouin zone corresponding to the primitive cell used in the present study. Example coordinates for a high symmetry path to sample the Brillouin zone are given in Tab. I. The band structure along the high symmetry path was plotted using the band interpolation method based on the maximally localized Wan-

TABLE II. Comparison between the experimental and theoretical lattice constants (in Å).

	Exp.[a]	Exp.[b]	Calc.[c]	Calc.[d]	Calc.[e]	Calc.[f]	Calc.[g]
a	12.214	12.233	12.287	12.27	12.31	12.438	12.289
b	3.0371	3.038	3.0564	3.03	3.08	3.084	3.0471
c	5.7981	5.807	5.823	5.80	5.89	5.877	5.8113
β	103.83	103.82	103.73	103.7	103.9	103.71	103.77

[a]Ref. 56.
[b]Ref. 65.
[c]This work, PBE.
[d]B88(exchange)+PW(correlation), Ref. 66.
[e]PBE, Ref. 67.
[f]PBE, Ref. 68.
[g]AM05, Ref. 10.

nier functions[62,63] as implemented in the software package WANNIER90[64]. We used s and p orbitals on both Ga and O atoms and performed disentanglement of the bands in a frozen energy window from -5 eV to 22 eV. The disentangled bands were also used for calculating the effective masses of the carriers. The bands were sampled in the range ± 0.005 Å^{-1} from the Γ point parallel to the crystal directions **a**, **b**, and **c**. Parabolic curves were used to fit the dispersions of the respective energy bands and the quadratic terms of the parabolas were converted to inverse effective mass tensor parameters as follows:

$$\left(m^{\star -1}\right)_{jj} = \frac{1}{\hbar^2}\frac{\partial^2}{\partial k_j^2}E(\mathbf{k}), \tag{8}$$

where derivatives are taken along directions $\mathbf{k} = k_j\hat{\mathbf{j}}$ with unit vector $\hat{\mathbf{j}}$, for example, parallel to **a**, **b**, or **c**.

Significant band-to-band transitions contributing to the dielectric tensor are identified by analyzing the matrix elements $|\mathcal{M}_{cv}|^2$ of the momentum operator between conduction and valence bands at the Γ point (Tab. V). The signatures (parallel or anti-parallel) of the projections of $|\mathcal{M}_{cv}|^2$ along the crystal directions **a** and $\mathbf{c}^*$ were obtained from inspecting the complex argument of $\mathcal{M}_{cv}$. Transition eigenvectors with parallel (antiparallel) arguments were respectively plotted in the first (second) quadrant of the Cartesian $(\mathbf{a} - \mathbf{c}^\star)$ plane.

IV. RESULTS AND DISCUSSION

A. Wavelength-by-wavelength analysis of the dielectric function tensor

Experimental and best match model calculated Mueller matrix GSE data is summarized in Figs. 3 and 4 for the (010) and $(\overline{2}01)$ surfaces, respectively. Selected data, obtained at 3 different sample azimuthal orientations 45° apart, and 3 angles of incidence (50°, 60° and 70°) are displayed. Panels with individual Mueller matrix elements are shown separately and arranged according to their indices. All Mueller matrix data are normalized to element M_{11}, therefore all GSE data have no units. For non-magnetic and non-chiral materials, in general, and as can be seen in the experimental and calculated data, Mueller matrix elements with symmetric indices can be obtained from simple symmetry operation, thus only the upper diagonal elements are presented. Data are shown for energies 0.75-9 eV except for M_{44} which only contains data from approximately 0.75-6.2 eV due to instrumental limitations of the VUV-VASE system. Data gathered from additional azimuthal orientations are not shown.

Each data set (sample, azimuthal orientation, angle of incidence) is unique, however, characteristic features are shared between them all at energies indicated by vertical lines. While we do not show all data in Figs. 3 and 4, we note that all data sets are identical when samples are measured at 180° rotated azimuth orientation. Most important to note in the experimental Mueller matrix data is the clear anisotropy shown by the nonzero off-diagonal block elements (M_{13}, M_{14}, M_{23}, M_{24}) and strong dependence on sample azimuthal orientation in all Mueller matrix elements. All data gathered by the measurement of multiple samples, with multiple orientations, and at multiple angles of incidence were analyzed simultaneously using a best-match model data regression procedure (polyfit). For each energy, up to 144 independent data points were included from 2 samples, 3 angles of incidence, and as many as 24 different azimuthal orientations. Only 8 independent model parameters for real and imaginary parts of ε_{xx}, ε_{yy}, ε_{zz}, ε_{xy} as well as 2 sets of energy-independent Euler angles describing the sample orientation and crystallographic structure and 2 roughness layer thickness parameters were fit for. The thickness parameters for the roughness layer of the (010) and $(\overline{2}01)$ samples were determined to be 1.78(1) nm and 1.61(1) nm, respectively. The best match model calculated Mueller matrix elements from the polyfit procedure are shown in Figs. 3 and 4 as red solid lines. We obtain an excellent agreement between model calculated and experimental Mueller matrix data. Euler angle parameters noted in the captions of Figs. 3 and 4 are in agreement with anticipated orientations of the crystallographic axes of each of the samples. The dielectric function tensor elements, ε_{xx}, ε_{yy}, ε_{xy}, and ε_{zz} determined from the wavelength-by-wavelength polyfit procedure are shown in Fig. 5, Fig. 6, Fig. 7 and Fig. 8, respectively, as dotted green lines.

B. CP model analysis

We identify 11 differentiable contributions in ε_{xx}, ε_{yy}, and ε_{xy}, and 5 in ε_{zz}. Distinct features can be seen, e.g., in the imaginary part of each tensor element in Figs. 5-8. Vertical lines are drawn corresponding to the results from our CP analysis at the respective CP transition energy model parameters. Note that while vertical lines

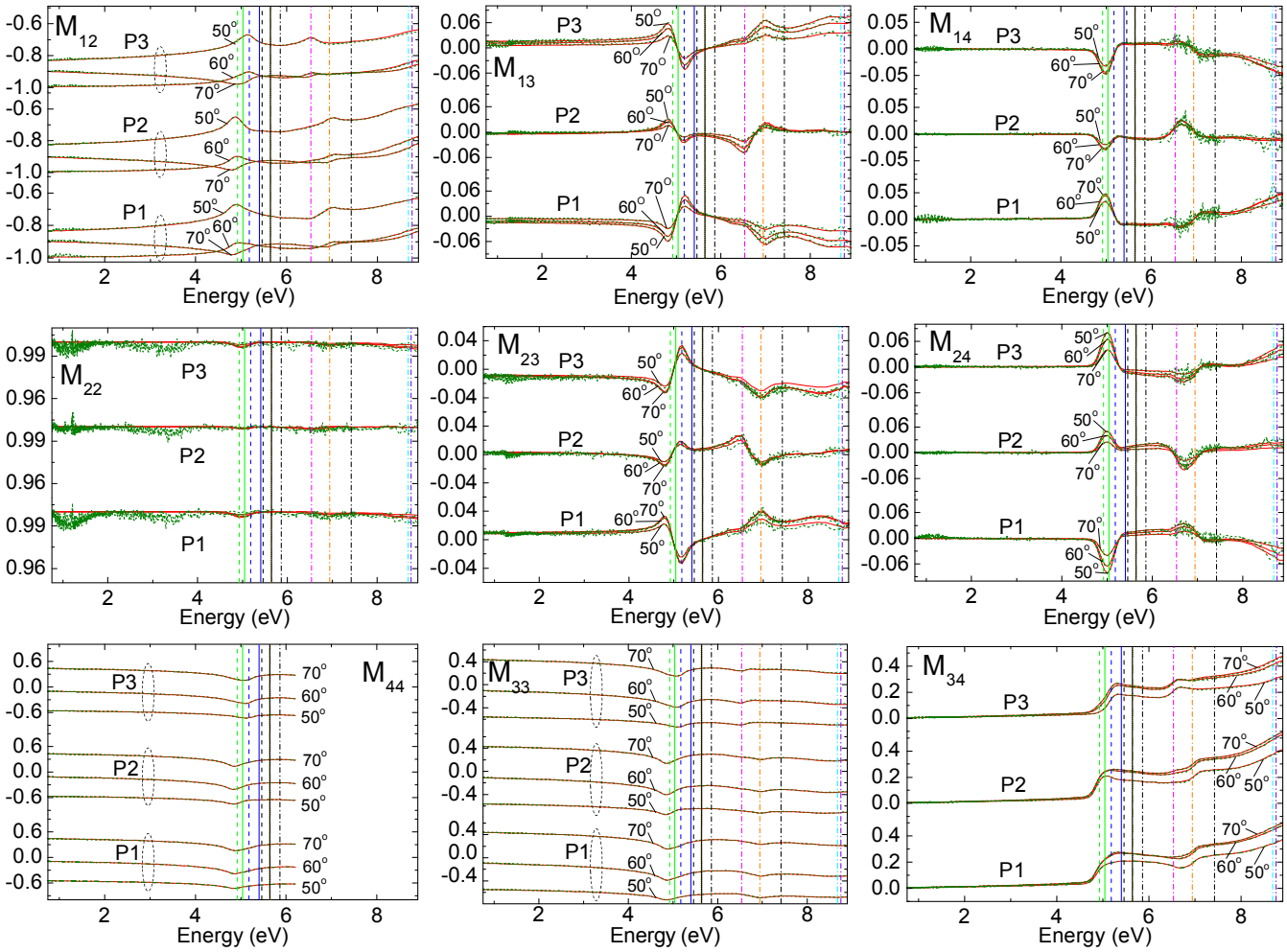

FIG. 3. Experimental (dotted, green lines) and best match model (solid, red lines) Mueller matrix data obtained from β-Ga_2O_3 (010) surface at three different azimuthal orientations (P1: $\varphi = 38.5(1)^\circ$, P2: $\varphi = 77.4(1)^\circ$, P3: $\varphi = 130.42(1)^\circ$). Data were taken at three angles of incidence ($\Phi_a = 50^\circ, 60^\circ, 70^\circ$). Vertical lines indicate energies at which CP transitions were suggested by the lineshape analysis. For color code and line styles of vertical lines, refer to Fig. 11. Euler angle parameters θ = -0.04(1)° and $\psi = 0.0(1)^\circ$ are consistent with the crystallographic orientation of the (010) surface. Note that angles of incidence in element M_{22} are not labeled as they are indistinguishable from each other.

are identical for ε_{xx}, ε_{yy}, and ε_{xy}, a different set is seen for ε_{zz} which corresponds to the difference between the monoclinic **a-c** plane and the axis parallel to **b**.[69]

a. ***a-c*** *plane* Eleven CP features are needed to match the tensor elements. Functions described in Sect. II C are used to model individual CP contributions as projections in the x-y plane with angular parameters $\alpha_{\mathrm{CP},j}$. The lowest band-to-band transition, $\mathrm{CP}_0^{\mathrm{ac}}$ was modeled with the HCP CP function (Eq. 4) with an excitonic contribution determined by an asymmetrically broadened Lorentzian oscillator (Eq. 5). It was assumed that excitonic and band-to-band transition contributions share the same unit eigenvector (angular parameter $\alpha_{\mathrm{CP},0}$). The excitonic CP contribution is labeled $\mathrm{CP}_{0x}^{\mathrm{ac}}$. We identify a second pair of CP contributions ($\mathrm{CP}_1^{\mathrm{ac}}$, $\mathrm{CP}_{1x}^{\mathrm{ac}}$, $\alpha_{\mathrm{CP},1}$) using the same functions. A Gaussian oscillator was used to model a very small CP contribution at 5.64 eV which could not be further differentiated ($\mathrm{CP}_2^{\mathrm{ac}}$, $\alpha_{\mathrm{CP},2}$). Above-band gap CP contributions ($\mathrm{CP}_{3-6}^{\mathrm{ac}}$, $\alpha_{\mathrm{CP},3-6}$) were identified at higher photon energies, which were modeled by asymmetrically broadened Lorentzian oscillators (Eq. 5). We were unable to differentiate between excitonic and band-to-band transition contributions associated with these higher energy CPs. Contributions due to higher-energy transitions, outside the investigated spectral region, were accounted for by a Gaussian function CP with projection along x ($\mathrm{CP}_7^{\mathrm{ac}}$), and y ($\mathrm{CP}_8^{\mathrm{ac}}$). The resulting best-match CP-MDF parameters are listed in Tab. III, and are shown as solid red lines in Figs. 5-7. An excellent agreement between our GSE wavelength-by-wavelength obtained and CP-MDF calculated data is noted. We also note close agreement with the GSE wavelength-by-wavelength obtained data reported by Sturm *et al.*

b. ***b*** *axis* Six CP features are needed to match the dielectric tensor element ε_{zz}. Functions described

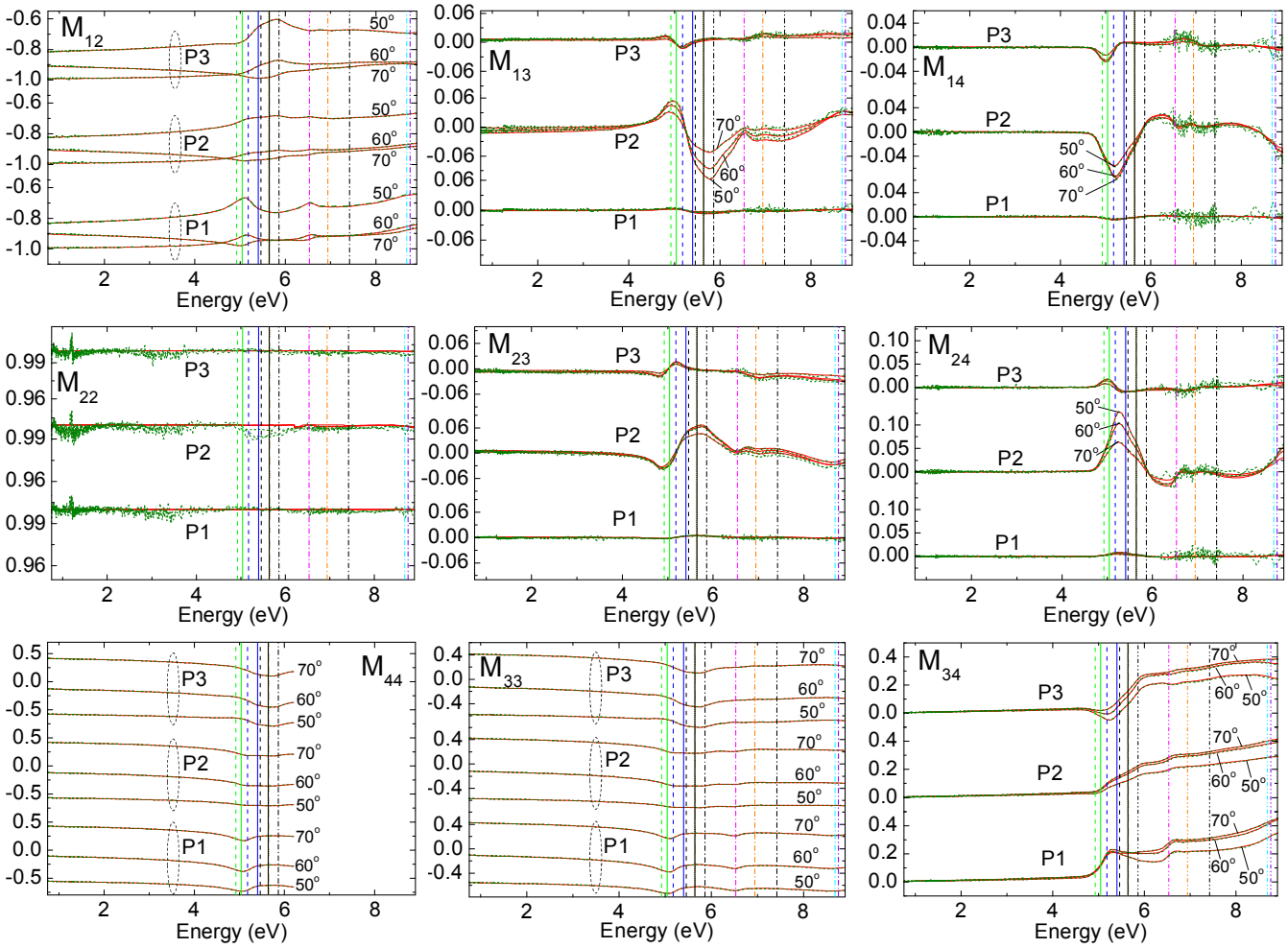

FIG. 4. Same as Fig. 3 except for β-Ga_2O_3 ($\bar{2}01$) surface. (P1: $\varphi = 184.3(1)^\circ$, P2: $\varphi = 228.9(1)^\circ$, P3: $\varphi = 266.7(1)^\circ$). Euler angle parameters $\theta = 89.97(1)^\circ$ and $\psi = -52.9(1)^\circ$ are consistent with the crystallographic orientation of the ($\bar{2}01$) surface. Note that angles of incidences are labeled wherever they are distinguishable.

in Sect. II C are used to model individual CP contributions projected along axis **b**. The lowest band-to-band transition, CP_0^b was modeled with the HCP CP function (Eq. 4; CP_0^b) with an excitonic contribution (CP_{0x}^b) determined by an asymmetrically broadened Lorentzian oscillator (Eq. 5). Above-band CP contributions (CP_{1-2}^b) were identified and modeled by functions in Eq. 5. Here again, we were unable to differentiate between excitonic and band-to-band transition contribution. Contributions due to higher-energy transitions, outside the investigated spectral region, were accounted for by a Gaussian function CP with projection along z (CP_{3-4}^b). The resulting best-match CP-MDF parameters are listed in Tab. IV, and are shown as solid red lines in Fig. 8. Again, an excellent agreement between our GSE wavelength-by-wavelength obtained and CP-MDF calculated data is noted. We also note close agreement with the GSE wavelength-by-wavelength obtained data reported by Sturm *et al.*

C. DFT analysis

1. *Band structure*

Figure 9 shows plots of the band structure at the DFT (PBE functional) and hybrid HF-DFT (Gau-PBE functional) levels of theory. The major difference between the two plots is the expected opening of the energy gap between the valence and conduction bands by about 2 eV. The most important feature, common to both plots, is the lowest conduction band which dominates the Brillouin zone center. A direct comparison between our band structures and previously published data is rather difficult as the majority of the authors only considered some of the high symmetry points in the first Brillouin zone. A band structure plotted using a comparable set of high symmetry points to the one used in the present work and also at the hybrid HF-DFT level was for example published by Peelaers and Van de Walle[70]. They used the HSE density functional with the fraction of HF exchange

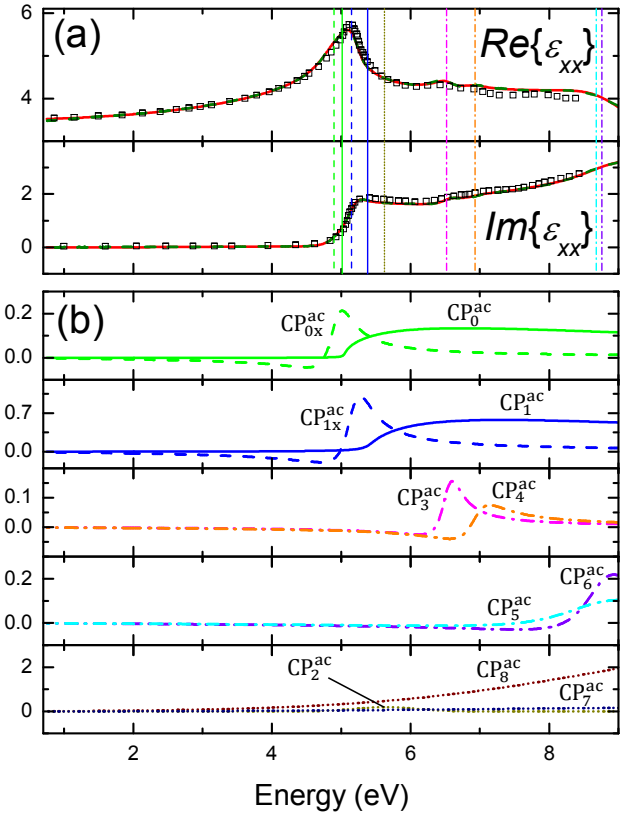

FIG. 5. (a) Dielectric function tensor element ε_{xx}, approximately along axis **a** in our coordinate system, obtained from wavelength-by-wavelength (polyfit) analysis (green dotted lines) and best match MDF analysis (red solid lines).Vertical lines indicate CP transition energy model parameters obtained from MDF analysis. Data from analysis by Sturm *et al.* are included for comparison (Ref. 9; open symbols). (b) Imaginary part of the individual CP contributions to the MDF used in this work are shown. For color code and line styles refer to Fig. 11.

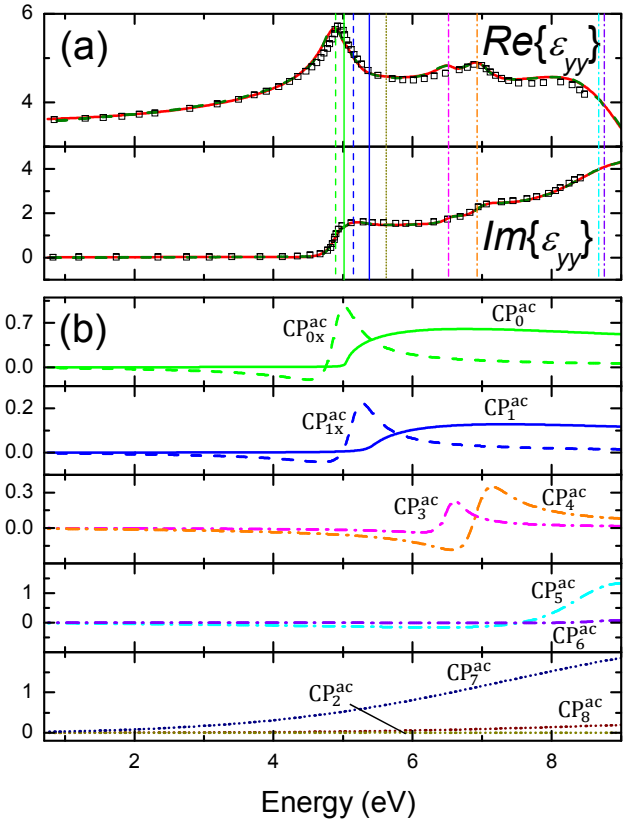

FIG. 6. Same as Fig. 5 for ε_{yy} approximately along axis $\mathbf{c}^*$.

TABLE III. CP-MDF parameters for polarization within the **a-c** plane of β-Ga_2O_3 obtained in this work from MMGE wavelength-by-wavelength data analysis of (010) and ($\bar{2}$01) surfaces of single crystalline bulk β-Ga_2O_3.

	α (°)	A (eV)	E (eV)	B (eV)	b (eV)
CP^{ac}_{0x}	115.1(1)	1.35(1)	4.92(1)[a]	0.40(1)	0.44(1)
[b]CP^{ac}_{0}	115.1(1)	25.9(4)	5.04(1)	0.02(1)	-
CP^{ac}_{1x}	25.2(1)	1.50(1)	5.17(1)[a]	0.43(1)	0.48(1)
[b]CP^{ac}_{1}	25.2(1)	28.0(5)	5.40(1)	0.09(1)	-
[c]CP^{ac}_{2}	174.2(2)	0.19(1)	5.64(1)	1.05(1)	-
CP^{ac}_{3}	50.4(1)	0.85(1)	6.53(1)	0.34(1)	0.11(1)
CP^{ac}_{4}	114.6(1)	0.88(2)	6.94(1)	0.56(1)	0.35(1)
CP^{ac}_{5}	105.4(1)	4.60(5)	8.68(1)	1.94(1)	2.24(4)
CP^{ac}_{6}	29.2(1)	1.45(4)	8.76(1)	0.97(2)	0.22(1)
[c]CP^{ac}_{7}	106.4(1)	2.34(1)	10.91(1)	8.28(1)	-
[c]CP^{ac}_{8}	17.6(1)	3.56(1)	12.54(1)	8.28(1)	-

[a]Energy calculated from binding energy model parameter.
[b]Denotes 3D M_0 Adachi function.
[c]Denotes Gaussian oscillator used in this analysis.

adjusted to reproduce an assumed value of the band gap. Their valence bands are very similar to ours, whereas their conduction bands are slightly shifted to higher energies and steeper than ours, most likely due to the effect of the higher amount of HF exchange included into the calculations (35% vs 24% in Gau-PBE).

The character of the band gap in β-Ga_2O_3 can be obtained from the band structure. The broad valence band maximum (VBM) has been reported previously along the L-I line of the Brillouin zone[70,71], slightly off the L point. Note again that in the current manuscript we use the nomenclature and labeling proposed by Setyawan and Curtarolo[61] with point L=[1/2,1/2,1/2], while in most previous publications this point is labeled M. Due to the fact that the valence band is very flat along the $L-I$ line, the actual location of the VBM can be easily missed. However, the energy difference between the actual VBM and, for example, the top valence band energy at the L-point only amounts to few meV. Thus studying the band properties at high-symmetry points L and at the Γ points is accurate enough. Local density approximation DFT methods typically predict the band gap to be indirect, and render the valence band at the L-point about 100 meV higher than the direct gap at Γ[71]. At the GGA-DFT level this difference is reduced to about 20-50 meV[10,66], and this usually holds for hybrid HF-DFT as well[10,27,70,72]. Our results at the Gau-PBE level show the

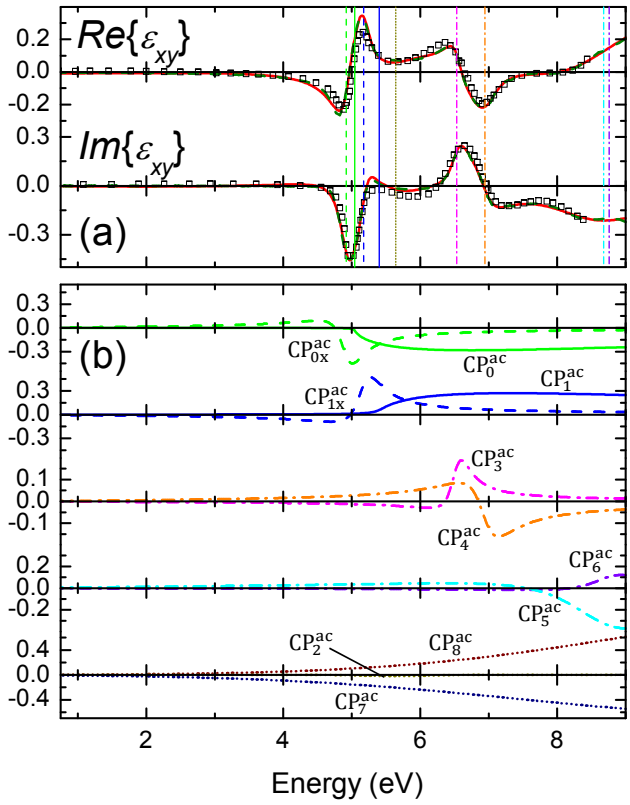

FIG. 7. Same as Fig. 5 for ε_{xy} within the **a-c** plane.

TABLE IV. Same as for Tab. III but for transitions polarized parallel to axis **b**.

	A (eV)	E (eV)	B (eV)	b (eV)
CP^b_{0x}	0.97(6)	5.46(3)[a]	0.54(1)	0.32(1)
[b]CP^b_0	64(2)	5.64(1)	0.11(1)	-
CP^b_1	1.24(6)	5.86(1)	0.50(2)	0.15(2)
CP^b_2	0.59(7)	7.42(3)	0.95(5)	0.08(1)
[c]CP^b_3	1.37(3)	9.53(1)	0.47(2)	-
[c]CP^b_4	3.50(1)	13.82(1)	8.86(1)	-

[a]Energy calculated from binding energy model parameter.
[b]Denotes 3D M_0 Adachi function.
[c]Transition outside investigated spectral region with limited sensitivity modeled with a Gaussian oscillator.

VBM near the L point about 50 meV higher than the top valence band at Γ. Interestingly, at the GW level (quasiparticle bands) the band gaps are completely degenerate, or even the direct gap appears marginally higher[10]. However, Ratnaparkhe and Lambrecht[73] used the quasiparticle self-consistent version of GW, QSGW[74], and obtained the indirect band gap energy smaller by nearly 100 meV than the direct band gap energy.

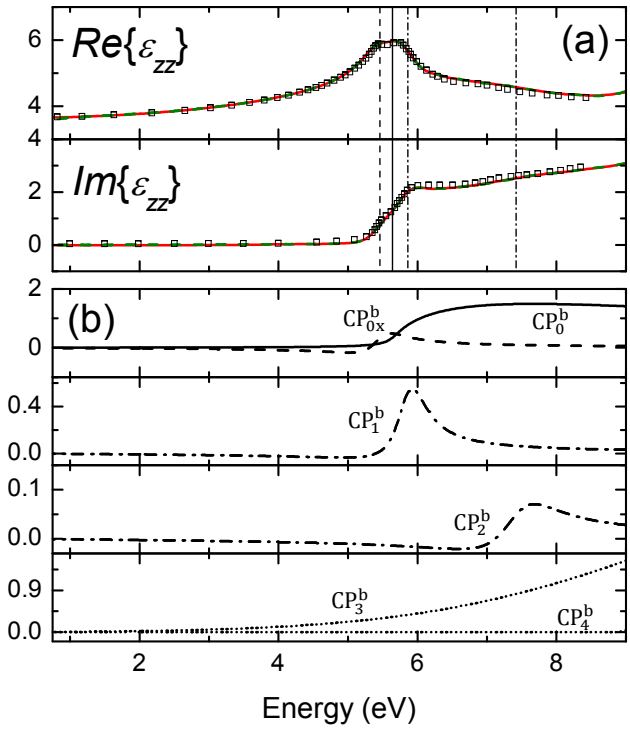

FIG. 8. Same as Fig. 5 for ε_{zz} approximately along axis **b**.

2. *Band-to-band transitions*

We analyze band-to-band transitions by identifying all allowed transitions, i.e., transitions with non-zero matrix elements of the momentum operator between conduction and valence bands, and whose transition energies are less than 10 eV. We find eight such transitions, summarized in Tab. V and Tab. VI, respectively, with polarization within the **a-c** plane and along axis **b**, respectively. The transition labels are according to the numbers of the bands involved, where numberings start at the top of the valence and at the bottom of the conduction bands. The matrix elements of the momentum operator are obtained from the overlap of the wavefunctions for the respective energy bands. Hence, their values represent the probabilities of the transitions, i.e., transition amplitudes, which can be compared to experimental ones. In the case of **a-c** plane transitions, which do not have any pre-defined orientation within the plane, the transition probabilities along the crystallographic directions **a** and **c*** constitute Cartesian components of the corresponding transition vectors, thereby defining the polarization direction of the band-to-band transition in space. Their orientations are shown in Fig. 12(b), and can be compared to the eigen dielectric displacement vectors obtained from GSE analysis. The fundamental (lowest energy) band-to-band transition is polarized nearly parallel to the crystallographic axis **c**. It is closely followed by a second transition polarized at a small angle from the crystallographic axis **a**. The lowest transition along the crystallographic axis **b** occurs about 0.6 eV above the fundamental transition

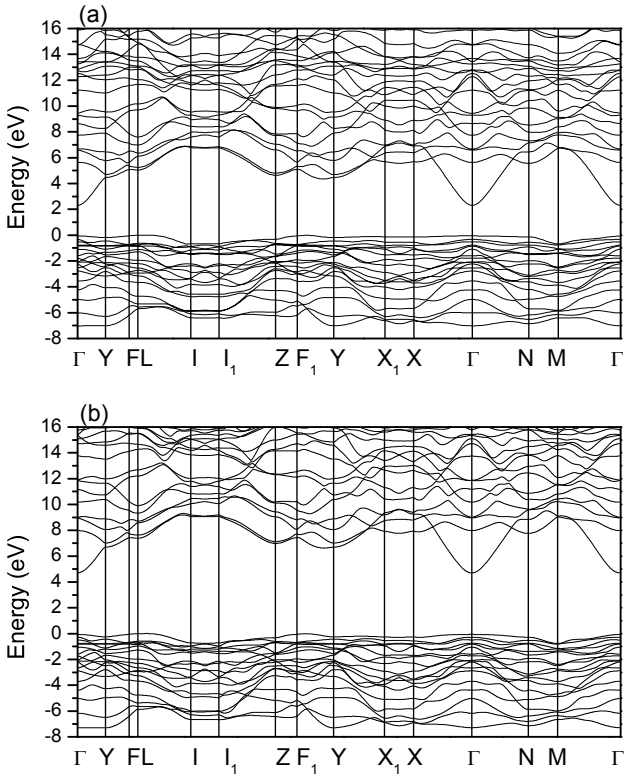

FIG. 9. Band structure of β-Ga_2O_3. (a) At the GGA-DFT (PBE) level; (b) at the hybrid HF-DFT (Gau-PBE) level.

TABLE V. Calculated band-to-band transition energies (E) within the **a-c** plane, and transition matrix elements $|\mathcal{M}_{cv}|^2_a$ and $|\mathcal{M}_{cv}|^2_{c^\star}$ projected onto axis **a** and $\mathbf{c}^\star$, respectively. Transitions are labeled Γ_{c-v} with indexes numbering bands upwards from the bottom ($c = 1$) of the conduction band and downwards from the top ($v = 1$) of the valence band at the Γ point. The polarization angle α is measured relative to axis **a**. Units of matrix elements are $(\hbar/\text{Bohr})^2$.

Label	E (eV)	$\alpha(^\circ)$	$\lvert\mathcal{M}_{cv}\rvert^2_a$	$\lvert\mathcal{M}_{cv}\rvert^2_{c^*}$	c	v
Γ_{1-1}	4.740	100.504	0.01972523	0.10638229	1	1
Γ_{1-2}	4.969	7.498	0.12773652	0.01681217	1	2
Γ_{1-7}	6.279	74.797	0.01304504	0.0480026	1	7
Γ_{1-11}	6.879	129.305	0.02598545	0.03174252	1	11
Γ_{2-3}	8.453	34.828	0.01417296	0.00986065	2	3
*Γ_{4-1}	9.0163	108.953	0.00011979	0.00034883	4	1
*Γ_{4-2}	9.2456	75.6222	0.00075006	0.00292599	4	2
Γ_{3-3}	9.432	88.912	0.0006232	0.03281954	3	3
Γ_{2-8}	9.679	81.108	0.01732007	0.11070298	2	8
Γ_{1-16}	9.714	5.4189	0.01139088	0.00108055	1	16

* Transition with small transition matrix element and disregarded in this work for CP model analysis comparison.

in the **a-c** plane. This tendency agrees well with GW results shown in Tab. VIII of Ref. 10.

TABLE VI. Same as Tab. V for polarization parallel axis **b**. Units of matrix elements are $(\hbar/\text{Bohr})^2$.

Label	E (eV)	$\lvert\mathcal{M}_{cv}\rvert^2$	c	v
Γ_{1-4}	5.350	0.06036769	1	4
Γ_{1-6}	5.636	0.14341762	1	6
Γ_{1-13}	7.472	0.00012693	1	13
Γ_{2-5}	8.680	0.02112952	2	5
Γ_{4-4}	9.626	0.00457146	4	4
Γ_{3-5}	9.658	0.00327158	3	5
Γ_{4-6}	9.912	0.00129364	4	6
Γ_{2-9}	9.991	0.08355157	2	9

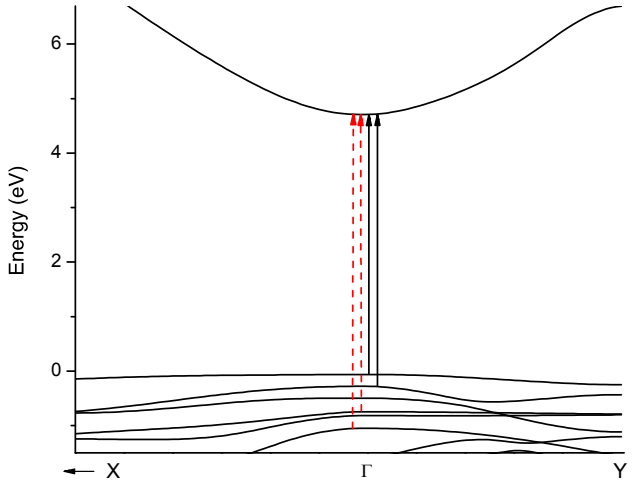

FIG. 10. (Color online) Band structure in the vicinity of the Γ point. Arrows indicate two lowest vertical band-to-band transitions polarized along the **b** axis (red dashed arrows) and within the **a-c** plane (black solid arrows). Note that the reciprocal space direction Γ-X corresponds to the real space directions parallel to the crystallographic vector **b**, and the reciprocal space direction Γ-Y corresponds to the real space direction lying within the **a-c** plane, inclined at a small angle from the crystallographic vector **a**.

3. Conduction and valence band effective mass parameters

Fig. 10 shows the vicinity of the Γ point of the Brillouin zone, with top valence bands and the first conduction band. The four lowest transitions are schematically shown as vertical arrows. The first conduction band is clearly parabolic, and rather symmetric, indicating a nearly isotropic electron effective mass, which is consistent with many previous studies[10,71]. It has been assumed previously[8] that due to the valence bands being generally flat, the hole effective masses are expected to be large, and that the electron effective mass parameter hence dominates the carrier reduced masses for the zone center band-to-band transitions. As can be inferred from Fig. 10, however, the valence band structure is far from isotropic. For example, the curvature of the second valence band in the direction $\Gamma - Y$, and the curvature of the fourth valence band in the direction $X - \Gamma$ are similar to the curvature of the first conduction band. The gen-

TABLE VII. Effective mass parameters for conduction (c) and valence (v) bands as indexed, and reduced effective mass parameter for lowest transition along directions $\hat{\mathbf{j}}$ in units of m_e.

$\hat{\mathbf{j}}$	$m^\star_{c1,jj}$ (m_e)	$m^\star_{v1,jj}$ (m_e)	$m^\star_{v2,jj}$ (m_e)	$m^\star_{v4,jj}$ (m_e)
a	0.224	1.769	0.466	6.649
b	0.301	$>10^a$	2.37	0.566
c	0.291	0.409	5.617	$>10^a$

[a] Band very flat in this direction

eral shape of these bands in different directions reveals a strong anisotropy.

a. Electron effective mass: The electron effective mass for β-Ga_2O_3 has been studied previously, both by computation and experiment. Computational results consistently predict a very small anisotropy, but span a relatively wide range of values: from $(0.12...0.13)m_e$ (GGA-DFT)[66], through $(0.23...0.24)m_e$ (local density approximation DFT)[71], to $0.39m_e$[75]. At the hybrid HF-DFT level the reported values are more consistent: $(0.26...0.27)m_e$[10], $(0.27...0.28)m_e$[27,70] with the HSE functional, and $0.34m_e$ for the B3LYP functional[72]. Our results (Gau-PBE) are presented in Tab. VII, which fall within this broad range of reported values, but exhibit a slightly higher anisotropy than found in previous studies.

b. Hole effective mass parameters: We have analyzed the effective mass parameters for the three valence bands involved in the lowest band-to-band transitions, and data are presented in Tab. VII. It is obvious that the hole effective mass anisotropy cannot be neglected for these bands. To our best knowledge, hole effective mass parameters at the Γ point have not been reported for β-Ga_2O_3 thus far. Yamaguchi[71] presented values of the top valence band effective mass parameter at point labeled "E" away from the zone center and thus not relevant for zone center transitions.

We note an interesting observation from our analysis here: The lowest values of the hole effective mass for each valence band occurs in the approximate polarization direction of the transition that connects this particular valence band and the lowest conduction band, and which we observe and identify from our GSE and DFT analyses. For the first and topmost valence band, the lowest value of the effective mass occurs along axis **c**, and the transition Γ_{1-1} is polarized nearly along axis **c** as well. For the second valence band, the lowest effective mass is along axis **a** and the transition Γ_{1-2} is polarized near axis **a**. For the fourth valence band the lowest hole effective mass is along **b** and the transition Γ_{1-4} is polarized along **b**. We thus observe here a clear correlation between the transition selection rules for electronic band-to-band transitions and the values of the carrier effective masses for these transitions. In contrast to previous studies, we find that not only do the hole effective mass parameters matter, but due to their very large anisotropy these parameters may play a decisive role for the polarization of the band-to-band transitions as well.

D. Comparison of DFT, GSE and literature results

Figure 11 summarizes energy levels below 10 eV determined by CP-MDF analysis and calculated by DFT in our work. Data from Sturm *et al.* are included for comparison. Overall, the agreement between our GSE and DFT results is excellent, in particular in the near-band-gap transition region, where number of observed transitions (4 in **a-c** plane, 3 along **b**) and their energy levels agree very well. At higher energies, individual transitions identified from DFT cannot be differentiated by GSE analysis, and appear as combined CP contributions.

a. ***a-c*** *plane:* CP-MDF and DFT transition energies are listed in Tables. III and V, respectively. In Fig. 11 we indicate a small contribution (CP_2^{ac} at 6.53 eV) for which we do not observe an equivalent transition in our DFT results. This energy is close to a strong contribution identified along axis **b**, and it appearance in the **a-c** plane may originate from lattice defects or from slight experimental misalignment. Figure 12 (a), (b) depict CP transition eigenvectors multiplied with their respective CP transition amplitude parameters, or transition matrix element, obtained from GSE and DFT, respectively. Colors and linestyles are as in Fig. 11, for convenient guiding of the eye. As one can see, the agreement between eigen dielectric displacement unit vectors in our CP-MDF approach and the polarization selection conditions obtained from DFT is remarkably good, in particular for the first two band-to-band transitions. None of the identified contributions are purely polarized along either axis **a**, **c**, or **c***. At higher energies we see a considerable shift between GSE and DFT. We attribute this to an increase in error associated with both the experimental results and the calculations at higher energies. The higher energy transitions predicted by DFT calculations which cannot be resolved from our GSE investigation are shown all in dark blue, the remaining colors correspond to the associated transitions identified by our GSE analysis. Previous work assumed transitions were independently polarized along crystallographic axes. We find here that the lowest two transitions are indeed polarized close to crystal axes **c** and **a**, respectively. Matsumoto *et al.* (Ref. 29) describe the onset of absorption at 4.54 eV and 4.56 eV for polarization along **c** and for polarization perpendicular to both **c** and **b**, respectively, also significantly lower than those found in this work. Ricci *et al.* (Ref. 26) reported absorption measurements and found the lowest onset occurring with polarization in the **a-c** plane at 4.5-4.6 eV, which is again at much lower energy than observed in this work. In these previous reports, the excitonic contributions were not considered. The closest comparison can be made with the CP-MDF analysis performed by Sturm *et al.* (Ref. 8). We find that the energy levels of the lowest excitonic contributions agree very well with those found

TABLE VIII. Energies and polarization eigenvector directions of the three lowest near-band gap CP transitions including excitonic contributions determined for monoclinic β-Ga_2O_3 in this work, in comparison with literature data. The polarization angle α in the **a-c** plane is defined between axis **a** and the respective transition dipole polarization direction.

	$E_{ac,0x}$ (eV)	$E_{ac,0}$ (eV)	α	$E_{ac,1x}$ (eV)	$E_{ac,1}$ (eV)	α	$E_{b,0x}$ (eV)	$E_{b,0}$ (eV)	α
This work	4.92(1)	5.04(1)	115.1(1)°	5.17(1)	5.40(1)	25.2(1)°	5.46(3)	5.64(1)	**b**-axis
Ref. 9[a]	4.88	5.15[b]	110°	5.1	5.37[b]	17°	5.41-5.75	5.68-6.02[b]	**b**-axis
Ref. 26[c]	-	4.4	**c**-axis	-	4.57	**a**-axis	-	4.72	**b**-axis
Ref. 29[c]	-	4.54	**c**-axis	-	4.56	⊥ to **c** and **b**	-	4.90	**b**-axis
This work DFT	-	4.740	100.504°	-	4.969	7.498°	-	5.350	**b**-axis
Ref. 10[d]	4.65	5.04	Mainly **c**	4.90	5.29	Mainly **a**	5.50	5.62	**b**-axis

[a] Ellipsometry.
[b] A fixed exciton binding energy parameter of 0.27 eV common to all 3 CP transitions listed here was assumed.
[c] Room temperature absorption edge.
[d] Theory.

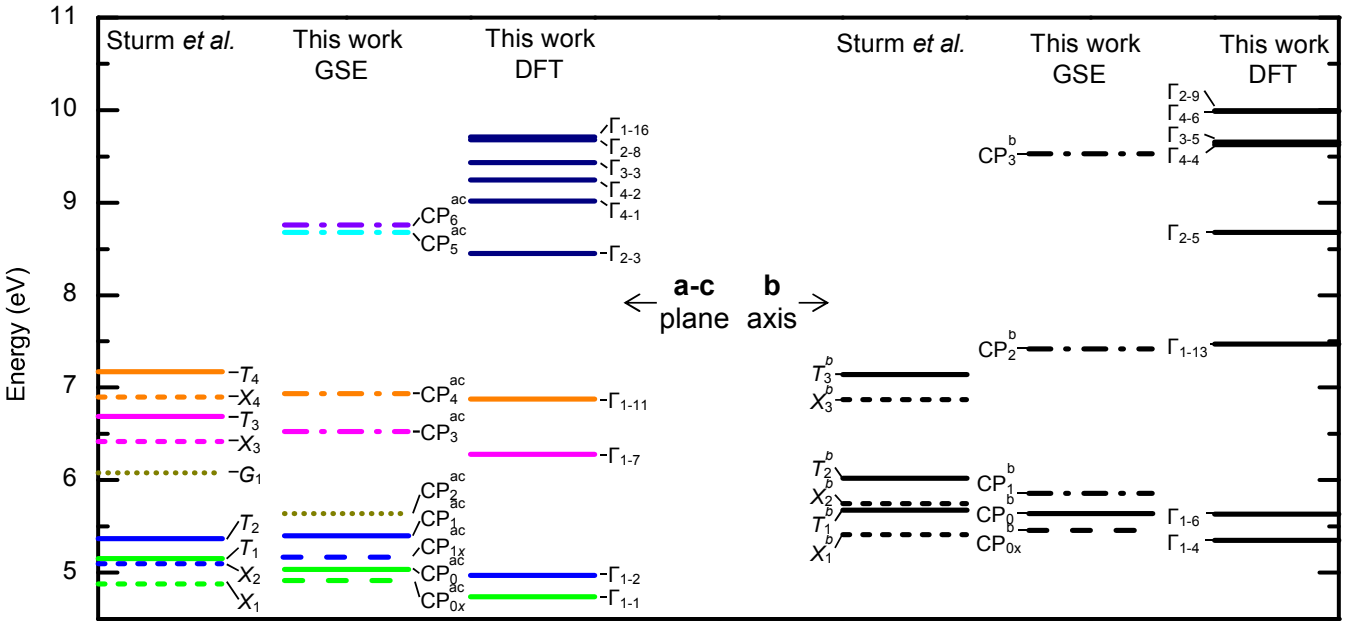

FIG. 11. Transition energies determined by CP-MDF analysis and calculated by DFT in our work, in comparison with data reported by Sturm *et al.* (Ref. 8). (Short-dashed (Sturm *et al.*) and dashed lines (this work): excitonic contributions; solid lines: near-band gap band-to-band transitions; dash-dotted lines: above-band gap transitions; dotted lines: higher energy transitions. For respective CP-MDF contributions see Sect. II C. DFT levels all refer to band-to-band transitions (solid lines). Color code for DFT **a-c** plane data are intended to match with order of energy levels identified in GSE CP-MDF analysis.)

in our work. However, because Sturm *et al.* imposed the constraint of fixed and uniform exciton binding energy parameters, we find in detail different band-to-band transition energy parameters is our work. Table VIII summarizes energy and polarization eigenvector directions of the near-band-gap transitions determined in this work in comparison with previous reports.

*b. **b** axis* CP-MDF and DFT transition energies are listed in Tables. IV and VI, respectively. Figure 11 summarizes transition energies obtained in this work, in comparison with data reported by Sturm *et al.*. Matsumoto *et al.* (Ref. 29) using reflectance measurements describe the onset of absorption around 4.9 eV with an absorption edge at 5.06 eV, slightly below our GSE value. Ricci *et al.* (Ref. 26) reported the onset of absorption occurring at approximately 4.8 eV. Energies reported by Sturm *et al.* (Ref. 8) are shifted in detail, which could be explained by the set binding energy constraint.

V. CONCLUSIONS

The eigen dielectric displacement model was applied for an analysis of β-Ga_2O_3 expanding into the vacuum ultra-violet spectral region. We differentiated 9 critical point contributions in the **a-c** plane, the lowest 2 of which were modeled with excitonic contributions. Additionally, we observed five critical point contributions in the **b** direction, with an excitonic contribution associated with the lowest transition. Additionally, transi-

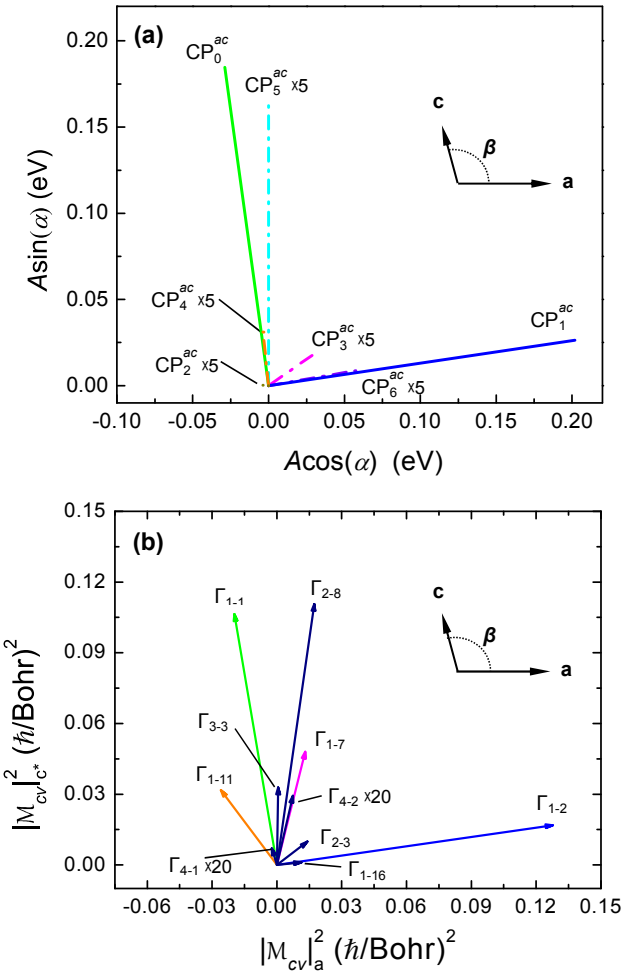

FIG. 12. Colors and lines styles as in Fig. 11. (a) Labels as given in Tab. III. MDF-CP transition eigenvectors, $\hat{\mathbf{j}} = \cos\alpha_j\hat{\mathbf{x}} + \sin\alpha_j\hat{\mathbf{y}}$, multiplied with their respective CP transition amplitude parameter, A. The amplitudes of the transitions have been normalized to the amplitude of the first transition, and the CP-MDF unit eigenvectors have been rotated by ≈17°. Small transition amplitude parameters are multiplied for convenience, as indicated. (b) Labels as given in Tab. V. DFT calculated transition matrix vector elements, $|\mathcal{M}_{cv}|^2_a$, $|\mathcal{M}_{cv}|^2_{c^\star}$. The magnitudes of the transition elements have been normalized by the vector magnitude of the first transition.

tions in the monoclinic plane, which does not contain any symmetry operation, were found to be distributed within the plane and none aligned with major crystal directions **a** or **c**. Our experimental analysis compares well with results from density functional theory calculations performed using a Gaussian-attenuation-Perdew-Burke-Ernzerhof density functional. From the analysis of the dielectric function we observe the same number of optical transitions in the energy range below 8 eV (below the continuum) as expected from DFT calculations in the same energy range for the Gamma point alone. Even though high symmetry points away from the Brillouin zone center give rise to additional Van-Hove singularities and potentially additional phonon-assisted band to band transitions, we can see no experimental evidence of additional transitions contributing to the measured dielectric function. As far as ellipsometry is concerned, beta-Ga2O3 is effectively a direct-bandgap material. We find that the effective masses for holes are highly anisotropic and correlate with the selection rules for the fundamental band-to-band transitions. The observed transitions are polarized close to the direction of the lowest hole effective mass for the valence band participating in the transition. The MDF approach and parameter set for β-Ga_2O_3 presented here will become useful for ellipsometry analysis of heterostructures, and may be expanded for description of alloys with monoclinic crystal symmetry.

VI. ACKNOWLEDGMENTS

We dedicate this work to our friend, colleague, and educator Professor Erik Janzén, who left us untimely and unexpected. We would like to thank Jürgen Furthmüller for useful discussions. This work was supported by the National Science Foundation (NSF) through the Center for Nanohybrid Functional Materials (EPS-1004094), the Nebraska Materials Research Science and Engineering Center (DMR-1420645), the Swedish Research Council (VR2013-5580), and the Swedish Foundation for Strategic Research (SSF, FFL12-0181 and RIF14-055). Partial financial support from NSF (CMMI 1337856, EAR 1521428), and J. A. Woollam Foundation is also acknowledged. DFT calculations were performed using the computing resources at the Center for Nanohybrid Functional Materials and at the Holland Computing Center at the University of Nebraska-Lincoln.

* Electronic mail: amock@huskers.unl.edu

[1] C. G. Granqvist, *Handbook of inorganic electrochromic materials* (Elsevier, 1995).

[2] U. Betz, M. K. Olsson, J. Marthy, M. Escola, and F. Atamny, Surface and Coatings Technology **200**, 5751 (2006).

[3] D. Gogova, A. Iossifova, T. Ivanova, Z. Dimitrova, and K. Gesheva, Journal of Crystal Growth **198???199, Part 2**, 1230 (1999).

[4] F. Réti, M. Fleischer, H. Meixner, and J. Giber, Sensors and Actuators B: Chemical **19**, 573 (1994).

[5] R. Roy, V. G. Hill, and E. F. Osborn, Journal of the American Chemical Society **74**, 719 (1952), http://dx.doi.org/10.1021/ja01123a039.

[6] H. H. Tippins, Phys. Rev. **140**, A316 (1965).

[7] J. F. Wager, Science **300**, 1245 (2003), http://science.sciencemag.org/content/300/5623/1245.full.pdf.

[8] C. Sturm, R. Schmidt-Grund, C. Kranert, J. Furthmüller, F. Bechstedt, and M. Grundmann, Phys. Rev. B **94**, 035148 (2016).

[9] C. Sturm, J. Furthmüller, F. Bechstedt, R. Schmidt-Grund, and M. Grundmann, APL Materials **3**, 106106 (2015).

[10] J. Furthmüller and F. Bechstedt, Phys. Rev. B **93**, 115204 (2016).

[11] P. Yu and M. Cardona, *Fundamentals of Semiconductors* (Springer Berlin Heidelberg New York, 2005).

[12] M. Schubert, J. A. Woollam, B. Johs, C. M. Herzinger, and B. Rheinländer, JOSA A **13**, 875 (1996).

[13] M. Schubert, Annalen der Physik **15**, 480 (2006).

[14] H. Fujiwara, *Spectroscopic ellipsometry: principles and applications* (John Wiley & Sons, 2007).

[15] M. Schubert, T. E. Tiwald, and C. M. Herzinger, Phys. Rev. B **61**, 8187 (2000).

[16] N. Ashkenov, B. N. Mbenkum, C. Bundesmann, V. Riede, M. Lorenz, D. Spemann, E. M. Kaidashev, A. Kasic, M. Schubert, M. Grundmann, G. Wagner, H. Neumann, V. Darakchieva, H. Arwin, and B. Monemar, Journal of Applied Physics **93**, 126 (2003).

[17] M. Schubert, C. Bundesmann, G. Jacopic, H. Maresch, and H. Arwin, Applied Physics Letters **84**, 200 (2004).

[18] M. Schubert, T. Hofmann, C. Herzinger, and W. Dollase, Thin Solid Films **455???456**, 619 (2004), the 3rd International Conference on Spectroscopic Ellipsometry.

[19] M. Dressel, B. Gompf, D. Faltermeier, A. Tripathi, J. Pflaum, and M. Schubert, Opt. Express **16**, 19770 (2008).

[20] O. Arteaga, A. Canillas, and G. E. J. Jr., Appl. Opt. **48**, 5307 (2009).

[21] T. Hofmann, D. Schmidt, and M. Schubert, in *Ellipsometry at the Nanoscale* (Springer, 2013) pp. 411–428.

[22] D. C. Qi, H. B. Su, M. Bastjan, O. D. Jurchescu, T. M. Palstra, A. T. S. Wee, M. Rübhausen, and A. Rusydi, App. Phys. Lett. **103**, 113303 (2013).

[23] M. Schubert, R. Korlacki, S. Knight, T. Hofmann, S. Schöche, V. Darakchieva, E. Janzén, B. Monemar, D. Gogova, Q.-T. Thieu, R. Togashi, H. Murakami, Y. Kumagai, K. Goto, A. Kuramata, S. Yamakoshi, and M. Higashiwaki, Phys. Rev. B **93**, 125209 (2016).

[24] A. Mock, R. Korlacki, S. Knight, and M. Schubert, Phys. Rev. B **95**, 165202 (2017).

[25] A. Kasic, M. Schubert, S. Einfeldt, D. Hommel, and T. Tiwald, Physical Review B **62**, 7365 (2000).

[26] F. Ricci, F. Boschi, A. Baraldi, A. Filippetti, M. Higashiwaki, A. Kuramata, V. Fiorentini, and R. Fornari, J. Phys.: Condens. Matter **28**, 224005 (2016).

[27] J. B. Varley, J. R. Weber, A. Janotti, and C. G. Van de Walle, Appl. Phys. Lett. **97**, 142106 (2010).

[28] A. Navarro-Quezada, S. Alamé, N. Esser, J. Furthmüller, F. Bechstedt, Z. Galazka, D. Skuridina, and P. Vogt, Phys. Rev. B **92**, 195306 (2015).

[29] T. Matsumoto, M. Aoki, A. Kinoshita, and T. Aono, Japanese Journal of Applied Physics **13**, 1578 (1974).

[30] T. Onuma, S. Saito, K. Sasaki, T. Masui, T. Yamaguchi, T. Honda, and M. Higashiwaki, Japanese Journal of Applied Physics **54**, 112601 (2015).

[31] C. Tanguy, Phys. Rev. B **75**, 4090 (1995).

[32] C. Tanguy, Solid State Communications **98**, 65 (1996).

[33] C. Tanguy, Physical Review B **60**, 10660 (1999).

[34] J. Heyd, G. E. Scuseria, and M. Ernzerhof, J. Chem. Phys. **118**, 8207 (2003); J. Chem. Phys. **124**, 219906 (2006).

[35] J. Paier, M. Marsman, and G. Kresse, Phys. Rev. B **78**, 121201(R) (2008).

[36] P. Deák, Q. Duy Ho, F. Seemann, B. Aradi, M. Lorke, and T. Frauenheim, Phys. Rev. B **95**, 075208 (2017).

[37] M. Schubert, Phys. Rev. Lett. **117**, 215502 (2016).

[38] M. Born and K. Huang, *Dynamical Theory of Crystal Lattices* (Oxford: Clarendon Press, 1954).

[39] M. Schubert and W. Dollase, Optics Letters **27**, 2073 (2002).

[40] T. E. Tiwald and M. Schubert, in *International Symposium on Optical Science and Technology* (International Society for Optics and Photonics, 2000) pp. 19–29.

[41] M. Schubert, B. Rheinländer, E. Franke, H. Neumann, J. Hahn, M. Röder, and F. Richter, Appl. Phys. Lett. **70**, 1819 (1997).

[42] D. Aspnes, J. Theeten, and F. Hottier, Physical Review B **20**, 3292 (1979).

[43] G. E. Jellison, M. A. McGuire, L. A. Boatner, J. D. Budai, E. D. Specht, and D. J. Singh, Phys. Rev. B **84**, 195439 (2011).

[44] C. W. Higginbotham, M. Cardona, and F. Pollak, Phys. Rev. **184**, 821 (1969).

[45] S. Adachi, T. Kimura, and N. Suzuki, J. Appl. Phys. (1993).

[46] C. F. Klingshirn, *Semiconductor Optics* (Springer Berlin Heidelberg New York, 1995).

[47] M. Grundmann, *The Physics of Semiconductors* (Springer, Berlin, 2006).

[48] C. Tanguy, Phys. Rev. Lett. (Erratum) **76**, 716 (1996).

[49] G. Irene and H. Tompkins, *Handbook of Ellipsometry* (Springer-Verlag GmbH Co. KG, 2004).

[50] D. D. S. Meneses, M. Malki, and P. Echegut, J. Noncryst. Sol. **352**, 769 (2006).

[51] M. Dressel and G. Grüner, *Electrodynamics of Solids* (Cambridge University Press, Cambridge, 2002).

[52] H. Aida, K. Nishiguchi, H. Takeda, N. Aota, K. Sunakawa, and Y. Yaguchi, Japanese Journal of Applied Physics **47**, 8506 (2008).

[53] K. Sasaki, A. Kuramata, T. Masui, E. G. Vìllora, K. Shimamura, and S. Yamakoshi,

Applied Physics Express **5**, 035502 (2012).
[54] K. Shimamura and E. Villora, Acta Physica Polonica, A **124**, 265 (2013).
[55] Quantum ESPRESSO is available from http://www.quantum-espresso.org. See also: P. Giannozzi, S. Baroni, N. Bonini, M. Calandra, R. Car, C. Cavazzoni, D. Ceresoli, G. L. Chiarotti, M. Cococcioni, I. Dabo, A. D. Corso, S. de Gironcoli, S. Fabris, G. Fratesi, R. Gebauer, U. Gerstmann, C. Gougoussis, A. Kokalj, M. Lazzeri, L. Martin-Samos, N. Marzari, F. Mauri, R. Mazzarello, S. Paolini, A. Pasquarello, L. Paulatto, C. Sbraccia, S. Scandolo, G. Sclauzero, A. P. Seitsonen, A. Smogunov, P. Umari, and R. M. Wentzcovitch, J. Phys.: Cond. Mat. **21**, 395502 (2009).
[56] J. Åhman, G. Svensson, and J. Albertsson, Acta Cryst. **C52**, 1336 (1996).
[57] J. P. Perdew, K. Burke, and M. Ernzerhof, Phys. Rev. Lett. **77**, 3865 (1996).
[58] H. J. Monkhorst and J. D. Pack, Phys. Rev. B **13**, 5188 (1976).
[59] J.-W. Song, K. Yamashita, and K. Hirao, J. Chem. Phys. **135**, 071103 (2011).
[60] J.-W. Song, G. Giorgi, K. Yamashita, and K. Hirao, J. Chem. Phys. **138**, 241101 (2013).
[61] W. Setyawan and S. Curtarolo, Comput. Mat. Sci. **49**, 299 (2010).
[62] N. Marzari and D. Vanderbilt, Phys. Rev. B **56**, 12847 (1997).
[63] I. Souza, N. Marzari, and D. Vanderbilt, Phys. Rev. B **65**, 035109 (2001).
[64] A. A. Mostofi, J. R. Yates, Y.-S. Lee, I. Souza, D. Vanderbilt, and N. Marzari, Comput. Phys. Commun. **178**, 685 (2008).
[65] K. E. Lipinska-Kalita, P. E. Kalita, O. A. Hemmers, and T. Hartmann, Phys. Rev. B **77**, 094123 (2008).
[66] H. He and M. A. B. R. Pandey, Appl. Phys. Lett. **88**, 261904 (2006).
[67] B. Liu, M. Gu, and X. Liu, Appl. Phys. Lett. **91**, 172102 (2007).
[68] S. Yoshioka, H. Hayashi, A. Kuwabara, F. Oba, K. Matsunaga, and I. Tanaka, J. Phys.: Condens. Matt. **19**, 346211 (2007).
[69] Note that separating a dielectric response into contributions from individual CP lineshapes can result in limited spectral regions with some individual model functions revealing negative imaginary parts. This observation is a consequence of coupling between individual processes, such as between band-to-band transitions and exciton formation. Such observations are often made in lineshape model approaches for the infrared optical properties in materials with coupled phonon modes.[76] Energy conservation is valid for the sum of all present physical processes only..
[70] H. Peelaers and C. G. V. de Walle, phys. stat. sol. (b) **252**, 828 (2015).
[71] K. Yamaguchi, Solid State Communications **131**, 739 (2004).
[72] H. He, R. Orlando, M. A. B. R. Pandey, E. Amzallag, I. Baraille, and M. Rérat, Phys. Rev. B **74**, 195123 (2006).
[73] A. Ratnaparkhe and W. R. L. Lambrecht, App. Phys. Lett. **110**, 132103 (2017).
[74] M. van Schilfgaarde, T. Kotani, and S. Faleev, Phys. Rev. Lett. **96**, 226402 (2006).
[75] M.-G. Ju, X. Wang, W. Liang, Y. Zhao, and C. Li, J. Mater. Chem. A **2**, 17005 (2014).
[76] F. Gervais and B. Piriou, J. Phys. C: Solid State Physics **7**, 2374 (1974).